UNIVERSITY OF CALIFORNIA,
IRVINE

A mm-Wave Receiver with Simultaneous Beamforming and MIMO Capabilities

DISSERTATION

submitted in partial satisfaction of the requirements
for the degree of

MASTER OF SCIENCE

in Electrical Engineering

by

Seyed Mohammad Hossein Mohammadnezhad

Dissertation Committee:
Professor Payam Heydari, Chair
Professor Michael M. Green
Professor Ozdal Boyraz

2018

TABLE OF CONTENTS

LIST OF FIGURES

LIST OF TABLES

ACKNOWLEDGMENTS

I would like to express my gratitude to my adviser for his continuous guidance and motivation.

Special thanks to Razieh Abedi and Amir Esmaili for their contribution to this work.

I would like to acknowledge GLOBALFOUNDRIES for facilitating the chip fabrication.

ABSTRACT OF THE DISSERTATION

A mm-Wave Receiver with Simultaneous Beamforming and MIMO Capabilities

By

Seyed Mohammad Hossein Mohammadnezhad

Master of Science in Electrical Engineering

University of California, Irvine, 2018

Professor Payam Heydari, Chair

This thesis presents analysis and design of overlapping multi-elements in a multi-stream beamforming-MIMO architecture to achieve higher beamforming and spatial multiplexing gains with lower number of elements compared to conventional architectures. As a proof of concept, a 4-element beamforming-MIMO receiver (RX) prototype operating at 64-67GHz[1] enabling 2-stream concurrent reception is designed and measured. By partitioning the RX elements into two clusters and partially overlapping these clusters to create two 3-element beamformers, both phased-array (coherent beamforming) as well as MIMO (spatial multiplexing) features are simultaneously acquired. 6-bit phase shifters (PSs) with 360° phase control and 5-bit VGAs with 11dB range are used to enable steering of the two RX clusters toward two arbitrary angular locations corresponding to two users. Fabricated in a 130nm SiGe BiCMOS process, the RX achieves a maximum direct conversion gain of 30.15dB and a minimum noise figure (NF) of 9.8dB across 548MHz IF bandwidth. S-parameter-based array factor measurements verify the interference suppression and spatial multiplexing in this partially-overlapped beamforming MIMO RX.

[1]The FCC's newly allocated 64-71GHz band for high-speed wireless links between small cells

Chapter 1

Introduction

There is an ever-increasing demand of high-speed communication for both wireless long to short-range [10] and wireline applications [6, 7]. The recent trend for facilitating high-speed communication has been to take advantage of the abundace of bandwidth available at higher frequencies. Multi-antenna architectures are essential at mm-wave frequencies to overcome excessive path loss and to facilitate reliable high data-rate, short-to-long range communication. Uncorrelated multi-antennas (MIMO) enhance data rate by simultaneous transmission of data streams through multiple independently faded channels. Additionally, coherently excited directive multi-antennas with dynamic beampatterns (phased arrays) enhance ergodic capacity by achieving higher SNRs. The theory of hybrid systems has recently been introduced to simultaneously attain the advantages of both MIMO and phased array. A conventional representation of a multi-cluster N-element hybrid is shown in figure 1.1, where each cluster, U_i, employs M dedicated phased-array elements. However, this approach may require excessive number of dedicated elements and high-complexity multi-stream digital baseband processing. A realization of hybrid has been introduced in [1]. This Cartesian combining RX inherently requires large number of splitters, multi-stage combiners, and mixers (e.g., 12 mixers for only 2-stream reception). Furthermore, the proposed RX suffers from

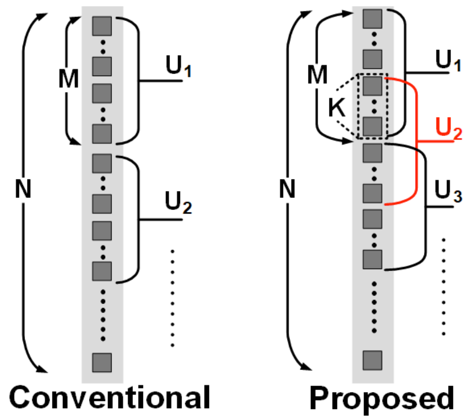

Figure 1.1: Conceptual presentation of a hybrid system and the proposed idea with partially-overlapped clusters

detrimental effects of too many cross-overs between signal paths. This complex architecture makes the design very challenging, if not impossible, at higher frequencies and seems impractical for higher number of streams.

To address these issues, this thesis presents the first partially-overlapped beamforming-MIMO RX operating in 64-67GHz[1] with independent amplitude and phase excitation for concurrent beamfroming and multi-stream reception, where N elements are partitioned into overlapped clusters of M beamforming elements with an arbitrary overlapping depth of K. Compared to a conventional hybrid, this idea achieves a higher MIMO multiplexing gain for a given number of phased-array elements per cluster. K and M are selected based on the trade-off between coherent processing and multiplexing gains required for a specific application.

[1]The FCC's newly allocated 64-71GHz band for high-speed wireless links between small cells

1.1 Baseband Design

Design of the baseband circuit is determiend by the required RF bandwidth, power budget and the intended application, ranging from few Hz and micro watts for biomedical application [15] to several GHz and watts for high speed wireless communications. Data converters are known to be the dominant source of power consumption at massive MIMO BS. To address the target data rates expected in 5G wireless communication, data converters with very fast sampling rates, high bit resolution and SFDR are required. ADC power consumption increases linearly proportional to sampling rate, f_s, and exponentially proportional to bit resolution, B.

However, it can be shown that distortion and receiver noise become trivial as the number of antennas increases [11]; therefore, dynamic power of massive MIMO can be reduced by a factor of $\sqrt{M}$ while the static power consumption at base station (BS) increases by a factor of M. It is proved in that with this scaling law design technique ADC bit resolution can be reduced by as high as $\frac{log_2 M}{2}$ while the power consumption of ADC, LNA, and Mixers can be reduced by a factor of $\sqrt{M}$ [11].

Based on this concept, an alternate method to designing costly high-speed ADCs is to design multiple sub-ADCs with low resolution (1 to 3 bits) for massive MIMO systems with many number of antennas. The capacity of a mm-wave MIMO system with one-bit quantization increases linearly with $log(N_{RX})$ for SIMO channel and linearly with $min\{N_{RX}, N_{TX}, L_{path}\}$ for MIMO channel, where N_{RX}, N_{TX}, L_{path} are the number of receiver, transmitter and multipath antennas respectively [12]. However, the non-linear distortion of low resolution ADCs will result in sub-optimal signal processing algorithms and enforces the use of more front-end antennas (at least 2 to 2.5 times more [13]) to compensate for the spectral efficiency loss. To combat such degradations, mixed-ADC architectures are suggested, where a small number of high resolution ADCs are included in addition to 1-bit ADCs resulting in less complex detection due to improved linearity of baseband [13].

At low SNR regimes, since system performance is not limited by SQNR (SQNR > SNR) increasing the number of RF chains is more effective in improving the data rate than going towards high resolution ADCs. At high SNR, the system data rate saturates due to integrated noise and system performance gets limited by achievable ADC resolution. Increasing the ADC resolution reduces the quantization noise compared to system noise and improves energy efficiency per achievable data rate. At higher ADC resolutions, limited improvement in data rate cannot compensate for exponential increase in power consumption and results in energy efficiency degradation [14].

1.2 Channel Estimation

To approach the capacity limit, knowledge of CSI at transmitter side is required. This way, hybrid beamforming designs can achieve performance close to *all-digital* architectures. CSI acquisition can be very costly. Furthermore, Increasing the number of antennas for mm-wave channels requires expensive spectral resources during CSI determination. At mm-wave frequency, CSI error due to pilot contamination is highly suppressed and CSI can be acquired based on ray-tracing model by estimation of AOD (angle of departure), AOA (angle of arrival), and paths gains.

Additionally, mm-wave channel exhibits spatial/angular sparsity and number of resolvable paths for both indoor and outdoor communication is very low (i.e. less than four) resulting in a low-rank channel response matrix. Therefore, due to low number of detectable paths, parameterized techniques such as interference cancellation (interference of clusters on each other) in addition to MUSIC algorithm[2] can be utilized to distinguish between multi-paths

[2]MUSIC algorithm utilizes the eigenvectors decomposition and eigenvalues of the multi-antenna covariance matrix for estimating AODs/DOAs of parallel data steam based on signal and noise subspaces.

(parallel data streams), then DOA (direction of arrival) and LS (least squared) methods can be used to estimate paths directions and paths gains respectively.

Using the interference cancellation in addition to MUSIC algorithm in detecting each path separately instead of approximating all the multi-paths parameters simultaneously results in higher suppression of additive noise in mm-wave channel and high resolution detection of angle directions for each cluster. Additionally, recent research suggests that in hybrid architectures by providing average CSI to RF beamformers and acquiring CSI for low-dimensional digital beamformers within each coherent fading block, CSI acquisition overhead can be relaxed and the system can still adopt to fast varying channels [7].

Once paths directions and gains are acquired, RF beamformers and VGAs can be configured to enhance beamforming gain and interference suppression within and between clusters to further maximize the capacity based on the acquired CSI.

Chapter 2

A Beamforming-MIMO Receiver

The proposed 4-element beamforming-MIMO RX for K=2, M=3, N=4 is shown in figure 2.2 [9]. These 4 elements are decomposed into 2 partially-overlapped clusters of 3-element beamformers to simultaneously steer the RX toward 2 arbitrary incident angles (Fig. 1(b)). Inter-element spacing within and between clusters in this architecture is set equal to $\lambda/2$, critical spatial sampling spacing, to avoid spatial aliasing in diversity beampatterns. Coherent processing gain within each cluster combined with spatial multiplexing gain from these 2 clusters improve reliability/diversity of high-rate multi-stream links at both low SNR (where performance is limited by energy-per-bit) and high SNR (where performance is set forth by channels degrees-of-freedom).

Two LNAs (LNA2-3), shared between U_1 and U_2, are followed by splitters to allow independent amplitude/phase control for these 2 clusters. The signals $U_{1k}e^{j\theta_{1k}}$ and $U_{2k}e^{j\theta_{2k}}$, 1⩽k⩽4, from distinct incident angles θ_1 and θ_2 appearing on 6 RF channels are fed to 6-bit phase shifters (PS) (ϕ_{ij} 1⩽i⩽2, 1⩽j⩽3) to be steered independently toward a desired angle. The phase-shifted signals are then fed to 5-bit VGAs (A_{ij} 1⩽i⩽2, 1⩽j⩽3) to suppress interference due to concurrent data reception of the other cluster by null steering technique explained in

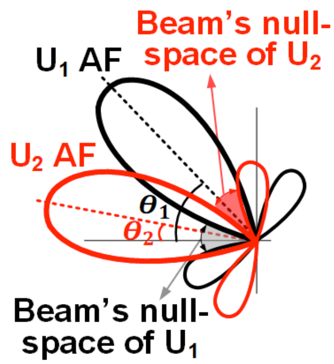

Figure 2.1: Spatial overlapping of two clusters array factor

section VI. Furthermore, any static amplitude or phase mismatch between RX's RF channels is compensated with high dynamic range of VGA and reference control of PSs. The VGAs' outputs within each cluster travel through carefully laid-out equi-length paths to a 3-to-1 combiner, where they are coherently power-combined at the desired incident angle ($U_{1(2)}e^{j\theta_{1(2)}}$ for cluster 1(2)) and suppressed at the undesired ($U_{2(1)}e^{j\theta_{2(1)}}$ for cluster 1(2)). A direct-conversion receveiver is designed. IQ mixers down-convert the RF signals at each combining node using a shared integrated LO network to be filtered and amplified in the baseband. To characterize RF channels, the RF signal at each cluster's combining node is monitored at the output of a tap coupler after differential to single-ended down-conversion with an on-chip balun. An 86-bit SPI is added on-chip to control tuning of phase shifter and VGA settings in addition to bias circuits.

Figure 2.1 shows an example scenario where the array factor of user 1 of cluster 1 shown in black is spatially multiplexed with the array factor of user 2 of cluster 2 shown in red. To enable spatial multiplexing, mainlobe of user 2 of cluster 2 is put on top of the null location of user 1 of cluster 1. Mainlobe and null location of cluster 1 are independetly set from mainlobe and null of cluster 2.

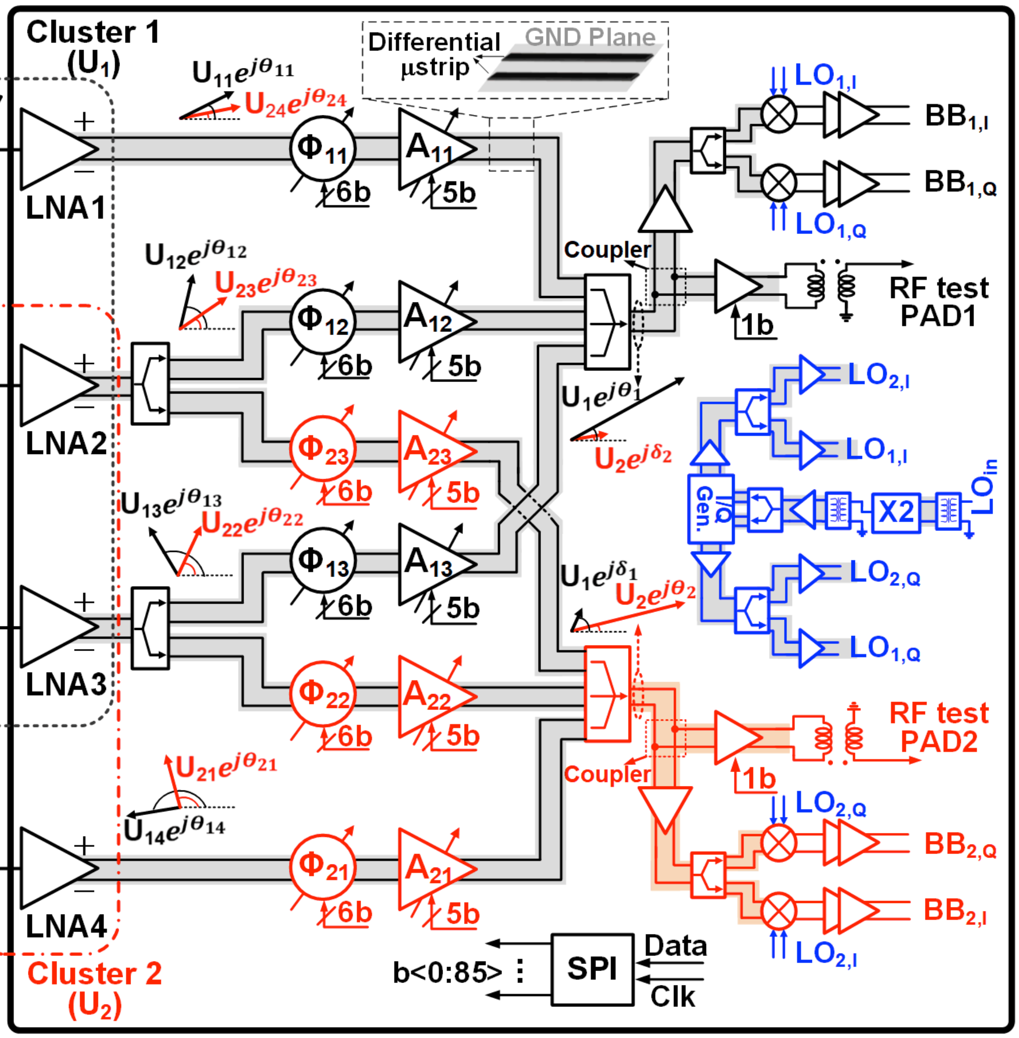

Figure 2.2: The 4-element realization of the beamforming-MIMO RX

Chapter 3

The Receiver RF Chain Design

A single RF channel from LNA to combiner input is shown in figure 3.1. Each RF-channel starts from an LNA front-end and passes through splitter, phase-shifter and VGA. After power combiner, a test output is taken to measure RF frequency response, VGA amplitude response and phase shifter phase response.

3.1 LNA

Each RF channel employs a 4-stage LNA. The first stage of LNA is an inductively degenerated common source stage to achieve simultaneous noise/power match. The first stage is

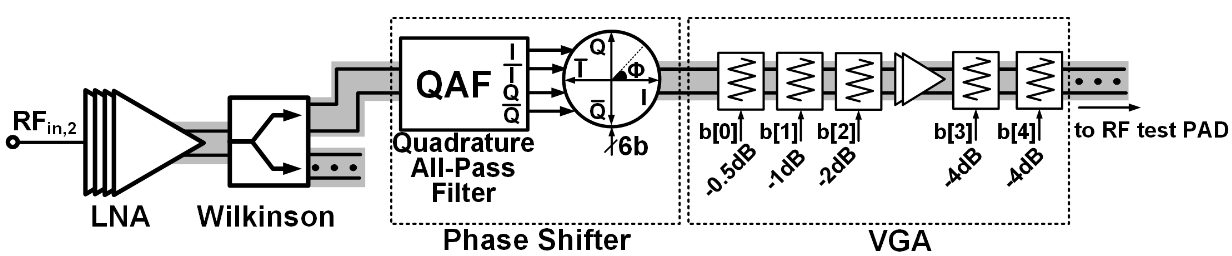

Figure 3.1: Single RF channel from LNA input to RF test PAD

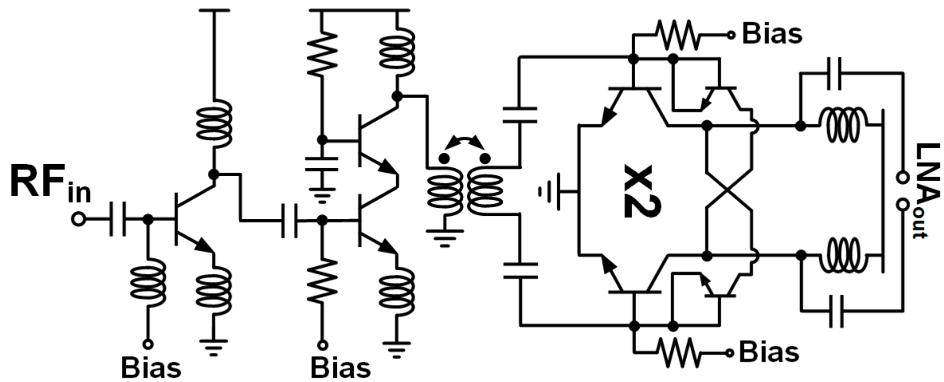

Figure 3.2: Schematic of 4-stage LNA

followed by a cascode stage designed for max available gain (MAG). After single-ended to differential conversion of RF input with an on-chip balun, the differential signal is fed to 2 neutralized differential stages to improve MAG and stability (figure 3.2).

3.2 Phase Shifter and VGA

Independent phase and amplitude controls at each RF channel were realized using 6-bit quadrature Gilbert-based PS and 5 passive π-stage. The PS QAF was de-Q'd to achieve pole-splitting and its characteristic impedance was optimized, considering the capacitive load seen by QAF, to compensate for IQ amplitude/phase errors and improve phase-linearity across a wider BW. An extra precision bit was added to PS DACs for fine tuning of phase states (figuer 3.3).

The measured 32 phase states of a single RF channel produced by 6-bit PS with 11.25° phase resolution is shown in figure 3.4, verifying a constant group delay and achieving RMS phase error better than 2.8° in the RF-BW.

The VGA incorporates inductors within and between π-stages to reduce RMS phase error across attenuation range and resonate out switches' parasitics (figure 3.5). Interstage amplifers are added within VGA's 2dB and 4dB steps to further compensate for the passive

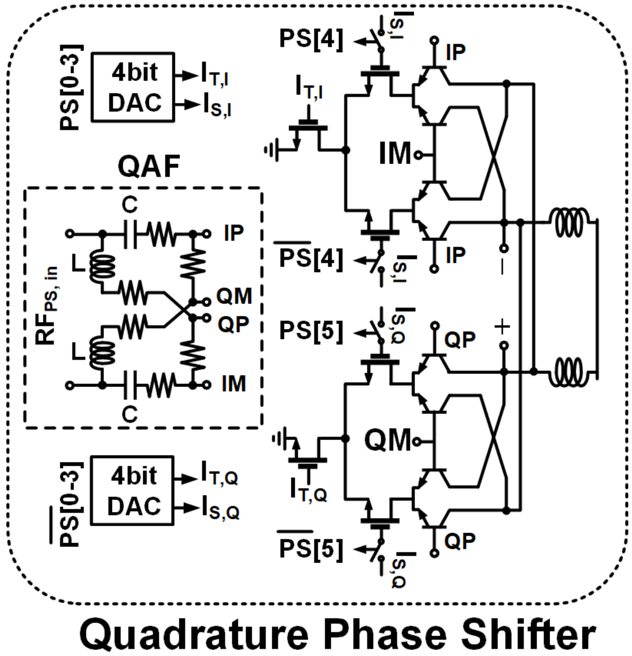

Figure 3.3: Schematic of quadrature Gilbert-based phase shifter

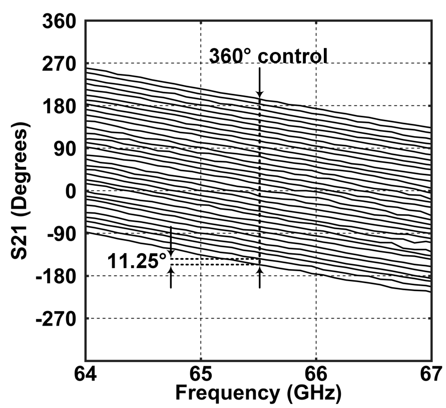

(a) Measured phase shifter response

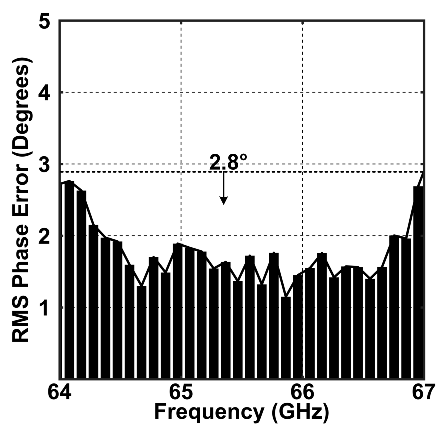

(b) Measured phase shifters RMS phase error

Figure 3.4: Measured phase shifter response and measured phase shifters RMS phase error

network's loss in off mode. The 5-stage VGA with interstage amplifiers achieves a measured 11dB dynamic range, while exhibiting RMS gain error smaller than 0.32dB in the RF-BW (figure 3.6).

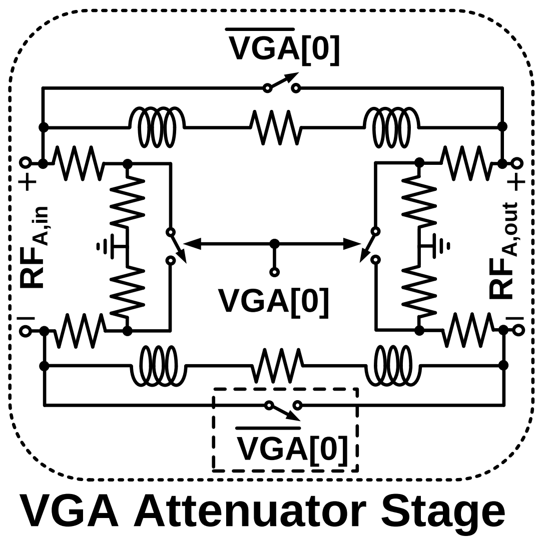

Figure 3.5: Schematic of passive π-stage VGA

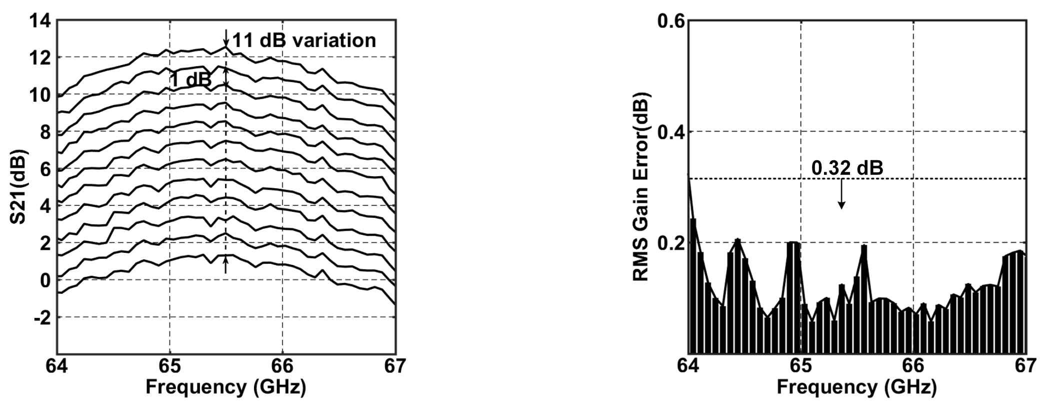

(a) Measured VGA steps

(b) Measured VGAs RMS gain error

Figure 3.6: Measured VGA steps and measured VGAs RMS gain error

3.3 Matching Network Design for Baluns

Fig. 3.7(a) shows the equivalent circuit of a balun, which is loaded with an input resistor R_1 and an output resistor R_2. An alternative circuit representation of a balun in terms of leakage inductor, magnetizing inductor, and an ideal balun is shown in Fig. 3.7(b). The resistor $R_1 = R_{P,C_1} \| R_{P,L_1} \| R_s$ captures the 50 Ω source resistor (R_S) in parallel with the loss of inductor $L_1(R_{P,L_1})$ and capacitor $C_1(R_{P,C_1})$. Likewise, the resistor $R_2 = R_{P,C_2} \| R_{P,L_2} \| R_L$ is comprised of 100 Ω load resistor (R_L) in parallel with the loss of inductor $L_2(R_{P,L_2})$

and capacitor $C_2(R_{P,C_2})$. The primary and secondary sides of the balun are tuned with capacitors C_1 and C_2, thereby enabling impedance matching on both sides and minimizing insertion loss. To realize a double-tuned balun, the primary and secondary sides should resonate at two distinct resonance frequencies $\omega_{r,1}$ and $\omega_{r,2}$, where $\omega_{r,1} = \omega_0 - \Delta\omega/2$ and $\omega_{r,2} = \omega_0 + \Delta\omega/2$, respectively. ω_0 represents the pass-band's center frequency and $\Delta\omega$ denotes the difference between the two resonant frequencies (see Fig. 3.7(c)). Assuming that the secondary side is already tuned at $\omega_{r,2}$, the primary side's component values are determined such that the primary side resonates at $\omega_{r,1}$. For $\Delta\omega < \sqrt{0.2}\omega_0$, the secondary impedance at $\omega_{r,1}$ is approximated as [8]:

$$Z_{sec}(\omega_{r,1}) \approx \frac{R_2}{1 - jQ_2\frac{2\Delta\omega}{\omega_0}} \tag{3.1}$$

where Q_2 is the loaded quality factor of the secondary side. The secondary impedance, $Z_{sec}(\omega_{r,1})$, at the primary's resonance frequency is inductive. Therefore, it is modeled as an equivalent series RL network (see Fig. 3.8), i.e.,

$$\begin{aligned} Z_{sec}(\omega_{r,1}) &= R_{sec}(\omega_{r,1}) + jL_{sec}(\omega_{r,1})\omega_{r,1} \\ R_{sec}(\omega_{r,1}) &= \frac{R_2}{1 + (Q_2\frac{2\Delta\omega}{\omega_0})^2} \\ L_{sec}(\omega_{r,1}) &= \frac{R_{sec}(\omega_{r,1})}{\omega_{r,1}} \times Q_2\frac{2\Delta\omega}{\omega_0} \end{aligned} \tag{3.2}$$

To cancel the imaginary part of the input impedance due to $L_1(1-K^2)$ and $L_{sec}(\omega_{r,1})$, C_1 needs to be:

$$C_1 = \frac{L_1(1-K^2) + n^2 L_{sec}(\omega_{r,1})}{\big[n^2 R_{sec}(\omega_{r,1})\big]^2 + \omega_{r,1}^2\big[L_1(1-K^2) + n^2 L_{sec}(\omega_{r,1})\big]^2} \tag{3.3}$$

where n is the effective turn ratio and K is the coupling factor. Assuming series resistive loss of the leakage inductance is negligible compared to $n^2 R_{sec}$, under input matching condition

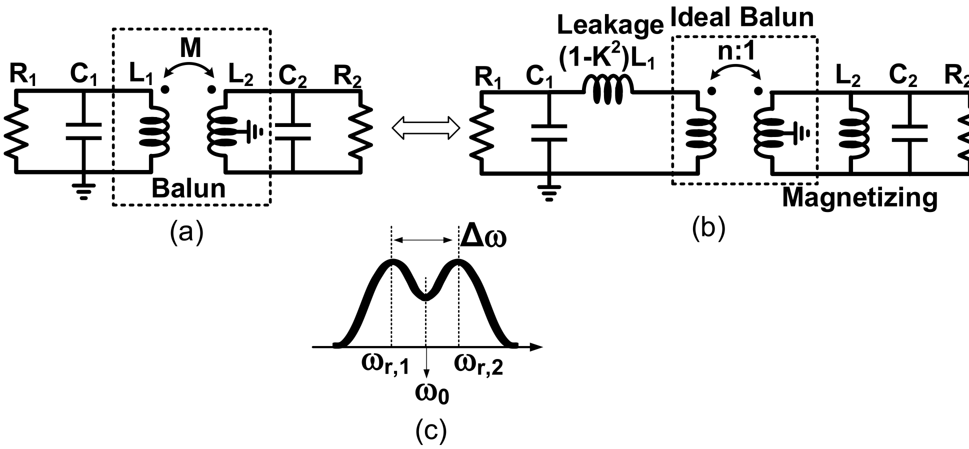

Figure 3.7: Circuit models for the loaded double-tuned baluns.

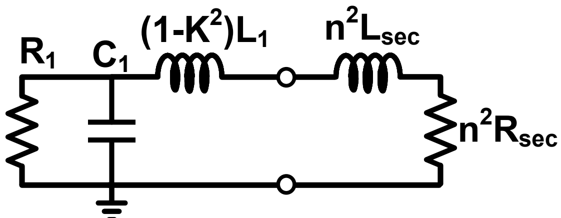

Figure 3.8: The equivalent circuit model form the primary side.

at $\omega_{r,1}$, L_1 is calculated to be:

$$L_1 = \frac{n}{\omega_{r,1}(1-K^2)} \times \sqrt{R_{sec}\left(\frac{R_{P,C_1}R_s}{R_{P,C_1}-R_s}\right) - n^2R_{sec}^2} - \frac{n^2L_{sec}}{1-K^2} \tag{3.4}$$

The value of L_1 will always be positive if the following inequality holds:

$$\Delta\omega < \frac{\omega_0}{2Q_2} \times \frac{\sqrt{1-K^2}}{K} \tag{3.5}$$

It is noteworthy that this inequality imposes a more stringent constraint on $\Delta\omega$ compared to $\Delta\omega < \sqrt{0.2}\omega_0$ for $K \geqslant 0.4$ and $Q \geqslant 2$. Hence, L_1 always assumes positive values. After calculating L_1 and C_1, L_2 is estimated by $L_2 = L_1\frac{K^2}{n^2}$. Moreover, C_2 is obtained to tune the secondary at $\omega_{r,2} = \omega_0 + \Delta\omega/2 = 1/\sqrt{L_2C_2}$.

3.4 Frequency Response of Double-Tuned Baluns

To improve bandwidth of the power splitter in this work, the frequency response of magnetically coupled tuned circuits is revisited. In particular, the normalized frequency response of a double-tuned balun is approximated as a function of the loaded primary/secondary quality factors, the coupling factor, and the pass-band's center frequency:

$$H_{norm}(\omega) \approx \left(\left[1-\frac{Q_1Q_2(\omega/\omega_0-\omega_0/\omega)^2}{1+K^2Q_1Q_2}\right]^2 + \left[\frac{2(\omega/\omega_0-\omega_0/\omega)\sqrt{Q_1Q_2}}{1+K^2Q_1Q_2}\right]^2\right)^{0.5} \tag{3.6}$$

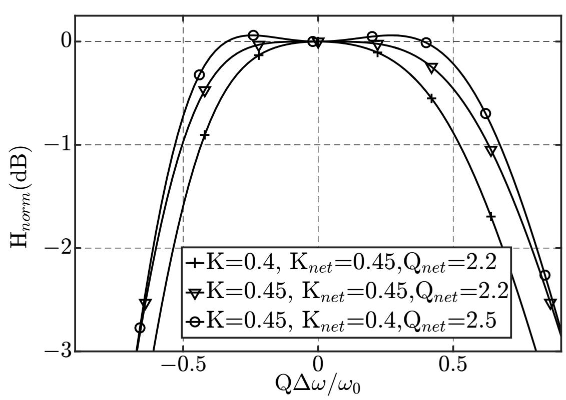

Figure 3.9: Frequency response of double-tuned balun.

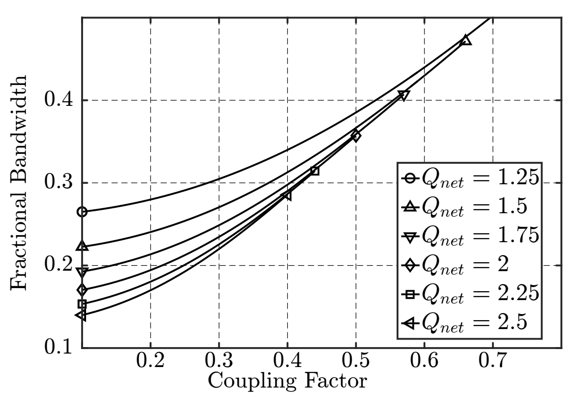

Figure 3.10: Fractional bandwidth as a function of coupling factor.

where Q_1 and Q_2 are the loaded quality factors of the primary and secondary, respectively. From Fig. 3.9, it is observed that the bandwidth increases with an increase in the coupling factor. It is proved that a double-tuned balun will assume a maximally flat response if and only if the coupling factor K becomes $K_{net} = 1/Q_{net} = \sqrt{0.5(1/Q_1^2 + 1/Q_2^2)}$. For $K > K_{net}$, the frequency response starts to show two peaks at $\omega_{r,1}$ and $\omega_{r,2}$. In other words, for $K > K_{net}$, increasing loaded quality factors Q_1 and Q_2 leads to wider separation of the two resonance frequencies and sharper pass-band to stop-band transition, and thus, wider bandwidth. This comes at the expense of larger in-band ripples. This behavior can be exploited to cascade multiple tuned circuits (e.g., multi-stage power splitters) so as to realize higher-order response with more degrees of freedom to better control the overall bandwidth, in-band ripple, and transition sharpness. For example, the first stage can be designed with coupling factor close to K_{net} to provide a flat frequency response, and the subsequent stages within the chain are designed at the same center frequency and slightly higher quality factor to compensate for the roll off of the first stage at higher frequency offsets from the center frequency. This method is eventually limited by the quality factors of primary/secondary inductors and tuning capacitors. The fractional bandwidth of two double-tuned circuits in cascade for coupling factors varying from 0.1 to K_{net} and for six different values of loaded quality factors between 1.25 and 2.5 is shown in Fig. 3.10. This figure clearly shows that for higher values of loaded quality factor, the fractional bandwidth increases with a higher slope as a function of coupling factor.

A max gain per channel of 12.3dB was measured from LNA input to RF test PAD at the center frequency of 65.5GHz with 3GHz RF-BW after VGA compensation for any gain or phase mismatch between RF channels. Gain or phase mismatch between different RF-channel are one-time calibrated before the start of measurements by VGA and phase shfiters. S_{21} outputs from LNA1 input to RF test PAD 1, LNA2 input to RF test PAD 1, LNA3 input to RF test PAD 1 are shown in figure 3.11a. The measured IP1dB is shown in figure 3.11b. The measureed worst-case IP1dB of RF channels is -16.3dBm at 65.5GHz. Upon down-

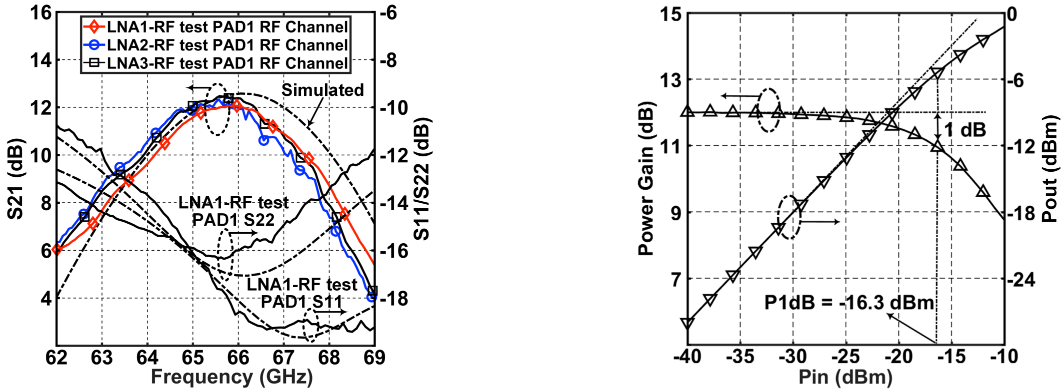

(a) Measured s-parameter of RF channels (simulated shown in dashed)

(b) The worst case measured IP1dB of an RF-channel

Figure 3.11: Measured s-parameter of RF channels and worst-case IP1dB

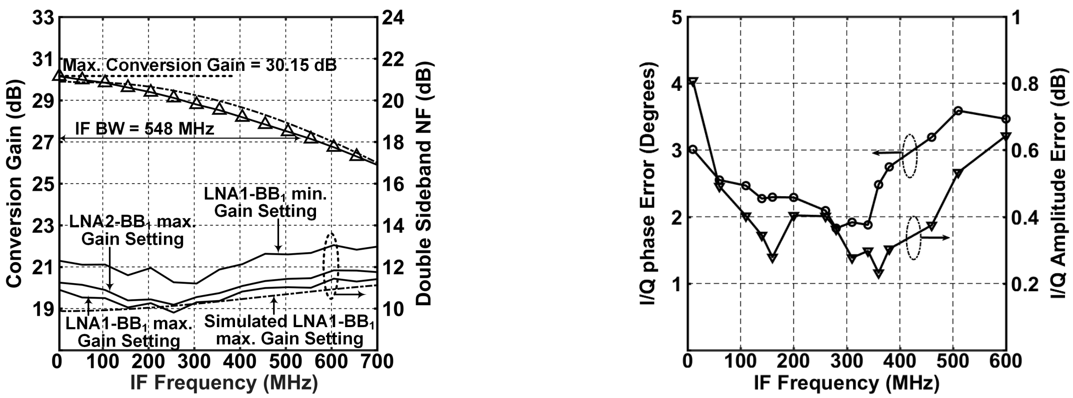

(a) Measured direct conversion gain and DSB NF from RF front-end to baseband (simulated shown in dashed)

(b) Measured I/Q phase errors and I/Q amplitude error across the baseband frequency from DC to 600MHz

Figure 3.12: Measured conversion gain, NF and I/Q phase and amplitude error

conversion, a conversion gain of 30.15dB was measured with 548MHz IF-BW. The measured DSB NFs for diffferent VGA settings are shown in figure 3.12a for min and max VGA settings of LNA1 input to BB1 output and LNA2 input to BB1 output. The measured DSB NF of a single RF-to-BB channel for these VGA attenuations varies from 9.8-11dB and 11.5-12.7dB, respectively, across the IF band of interest. The IQ amplitude/phase errors were measured to be less than 0.8dB/3.6° across the IF-BW (3.12b).

Chapter 4

Inter-element Coupling

Inter-element couplings within or between clusters have been investigated, as they can increase gain/phase error at combining nodes. Sources of coupling between adjacent RF channels, RF channel 1 and 2 and RF channel 2 and 3 of cluster 1 are depicted in figure 4.1 and 4.2 respectively. Coupling paths between these two RF channels include:

(a) last single-ended stage of LNA3 to the input of LNA2

(b) after phase shifter ϕ_{13} to ϕ_{23}

(c) after VGA A_{13} to to ϕ_{23} or A_{23}

the coupling signal power after passing through these three different paths are given by:

(a) $P_{coupled,a} = (Gain_{LNA3}Gain_{LNA2}Gain_{phi_{12}}A_{12})P_{sig}$

(b) $P_{coupled,b} = (Gain_{LNA3}Gain_{\phi_{13}}Gain_{\phi_{12}}A_{12})P_{sig}$

(c) $P_{coupled,c} = (Gain_{LNA3}Gain_{\phi_{13}}A_{13}Gain_{\phi_{12}}A_{12})P_{sig}$

Coupling path (case a) is the dominant source of coupling in the designed receiver, where

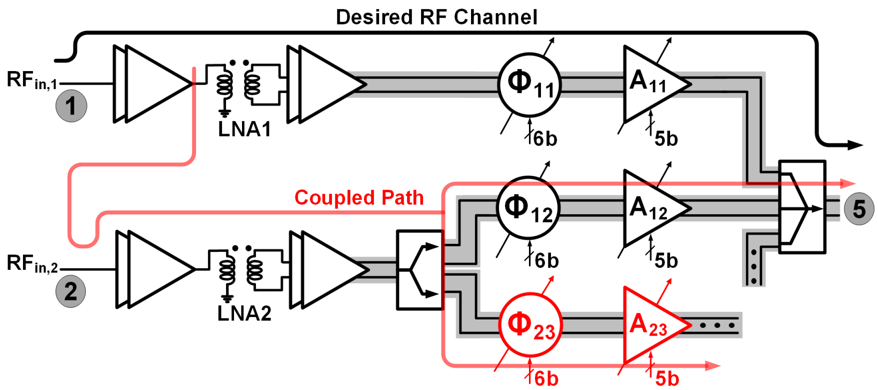

Figure 4.1: Coupling path between RF channels 1 and 2 of cluster one

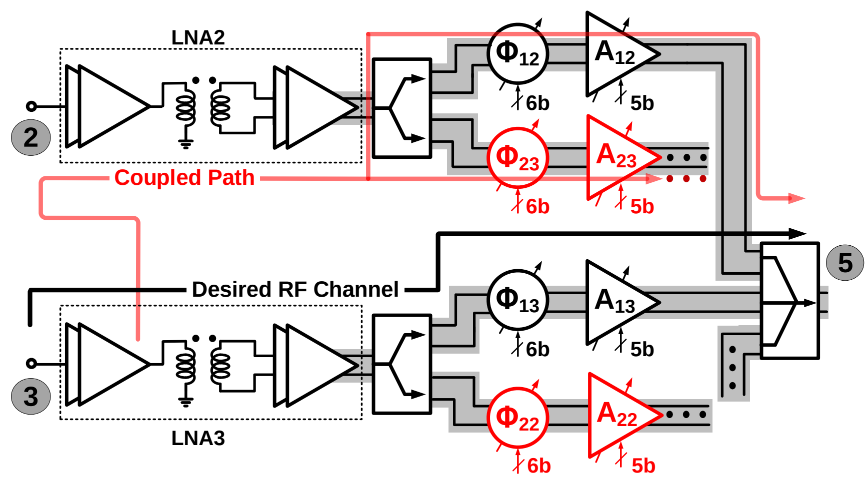

Figure 4.2: Coupling path between RF channels 2 and 3 of cluster one

the signal at the last single-ended stage of LNA3 couples to the input of LNA2 and after getting amplified by both LNA2 and LNA3 passes through the undesired RF channel 2 of cluster 1 and appears at the combining node of cluster 1.

Bypass rails between RF channels of these two clusters heavily suppress the coupling from differential phase shifter to phase shifter (case b) or differential VGA to phase shifter of VGA (case c).

In order to measure coupling effect between RF channels 2 and 3 of cluster 1, ϕ_{13} is set as reference phase and ϕ_{23} and ϕ_{12} are adjusted to four different values of zero, $\pi/2$, π, and

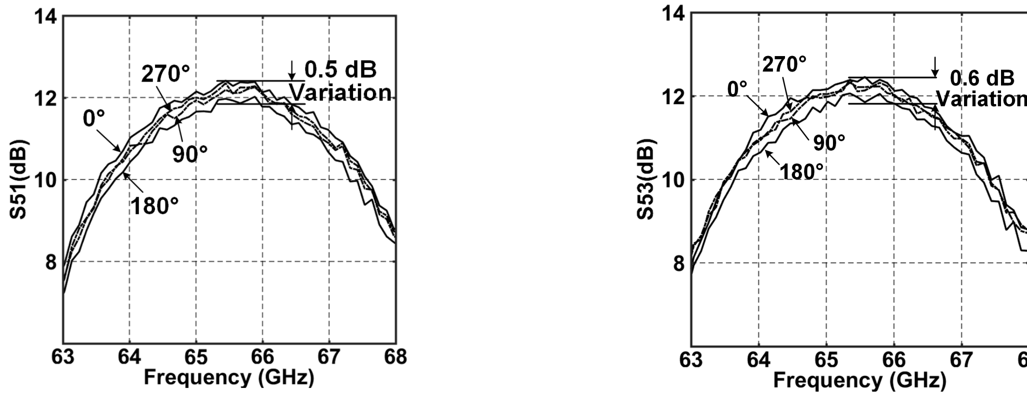

(a) Measured undesired gain variations for different phase shifter settings due to coupling between channel 1 and 2

(b) Measured undesired gain variations for different phase shifter settings due to coupling between channel 2 and 3

Figure 4.3: Measured undesired gain variations for different phase shifter settings due to coupling between RF channels 1 and 2 and RF channels 2 and 3

$3\pi/2$.

Phase differences of zero and π result in maximum gain error and $\pi/2$ or $3\pi/2$ result in maximum phase error after cluster combining. Figure 4.5a and 4.5b shows the measured RMS phase/gain error at the combing node due to channel 2 and 3 coupling across all phase states. The measured RMS gain/phase errors due to coupling are less than 0.56dB/1.4° in the RF-BW.

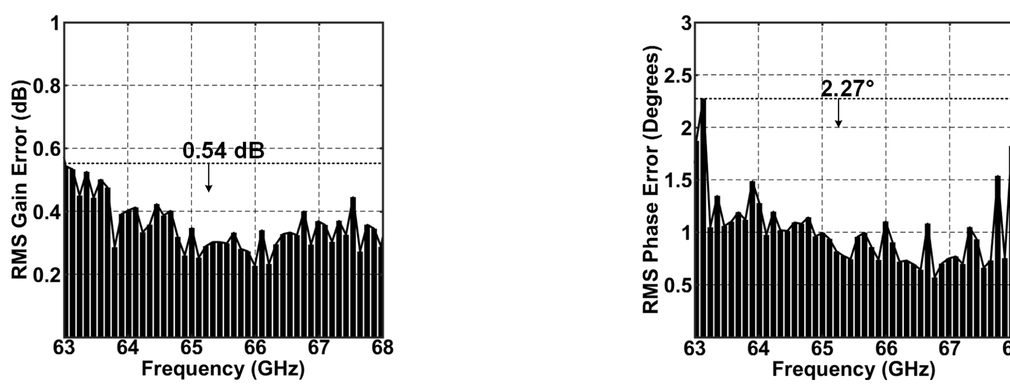

(a) Quadrature Gilbert-based phase shifter

(b) passive π-stage VGA

Figure 4.4: RMS gain and phase error due to coupling between RF channel 1 and 2

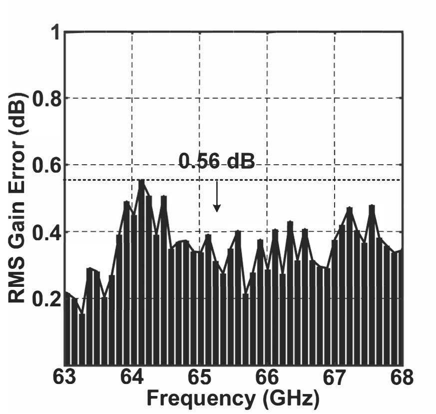

(a) Quadrature Gilbert-based phase shifter

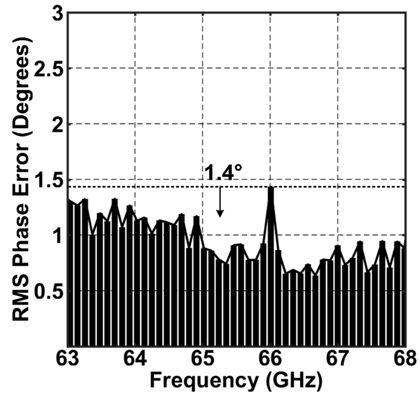

(b) passive π-stage VGA

Figure 4.5: RMS gain and phase error due to coupling between RF channel 2 and 3

Coupling can also happen from RF channel 1 to RF channel 2 of cluster 1 or 2. Dominant source of coupling is again from the last single-ended stage of LNA1 to the input of LNA2, where the signal sees a gain of $Gain_{LNA1}Gain_{LNA2}Gain_{\phi_{23}}A_{23}$ and appears at the combining node.

The dominant source of coupling is depicted in figure 4.1, occurring between closest adjacent RF channels (LNA1-ϕ_{11}-A_{11} and LNA2-ϕ_{12}-A_{12}) where the output of the last single-ended stage of LNA1 couples to the input of LNA2 and after amplification will introduce gain/phase errors at port 5. S_{51} is measured when coupled and desired RF channels are turned on, ϕ_{11} is set at reference, and ϕ_{12} and ϕ_{23} are set to zero or π to measure max gain error, and $\pi/2$ or $3\pi/2$ for max phase error, while keeping ϕ_{11} constant at $0°$. Gain variation due to coupling between RF channels 1 and 2 for 4 different phase settings is shown in figure 4.3a. To lower these errors, low-impedance bypass rails were placed between adjacent channels and dedicated VCC/GND planes were designed for single-ended stages. The measured RMS gain/phase errors due to coupling are less than 0.54dB/2.27° in the RF-BW (figures 4.4a and 4.4b).

Chapter 5

Null Steering and Spatial Multiplexing

Beam-shaping of each cluster's array factor (AF) by adjusting PS and VGA settings allows spatial multiplexing of these clusters. The null location for each cluster is steered with VGA steps, enabling each cluster to suppress interferences at undesired incident angles located in its null space, particularly at mm-wave where angular spread at angle of arrival is narrow. Normalized AF extracted from s-parameter measurements of RF channels within each cluster for 512 VGA settings are shown in figure 5.1, and compared with the ideal AF. The AF plot for a subset of VGA settings under a constant array gain is shown in figure 5.2, which demonstrates the trade-off between beamwidth and sidelobe level upon null-steering. Shown in 5.3 is the measured spatially multiplexed AFs of 2 clusters steered concurrently toward exemplary angles of $\theta_1 = 60^\circ$ and $\theta_2 = 90^\circ$, where VGAs in each cluster were configured to achieve better than 20dB interference suppression from the other cluster. The measured phase steering capability of each phased-array cluster is shown in 5.4. The measured signal-to-interference ratio (SIR) at the combining node of a 3-element cluster with its AF steered toward broadside is shown in 5.5, where the incident angle of interference is swept from 5°

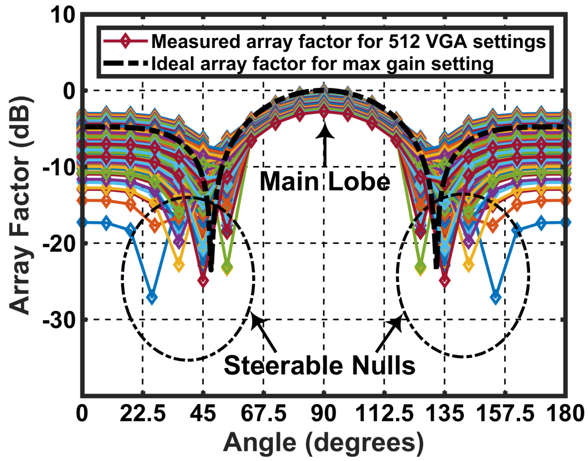

Figure 5.1: Measured array factor of each cluster for 512 VGA settings

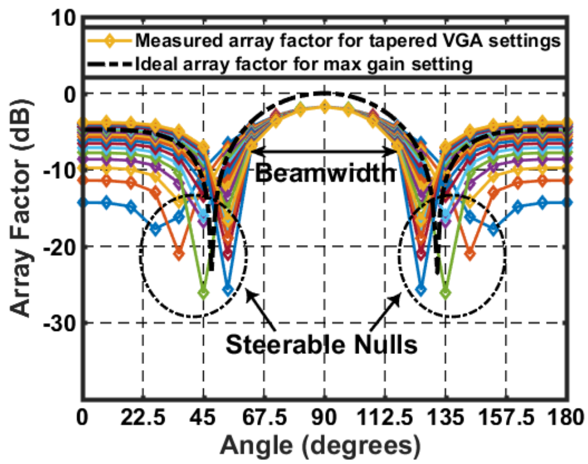

Figure 5.2: Measured array factor of each cluster for constant array gain

to 175° with 15° steps. To test the RX robustness to angle estimation errors, a ±LSB/2 (= ±5.625°) error is introduced to each step. An SIR $\geqslant$ 15dB was achieved across wide null-steering intervals (22.5°-74° and 106°-157.5°) due to 11dB dynamic range of the VGA. To further extend this interval and capture undesired incident angles as close as HPBW/4 from the desired incident angle, the main-lobe of the desired angle is slightly offset from broadside (max offset $\leqslant$ HPBW/4). It is noteworthy that by increasing the number of elements, SIR and null steering interval can be enhanced due to narrower HPBW and higher suppression of sidelobes.

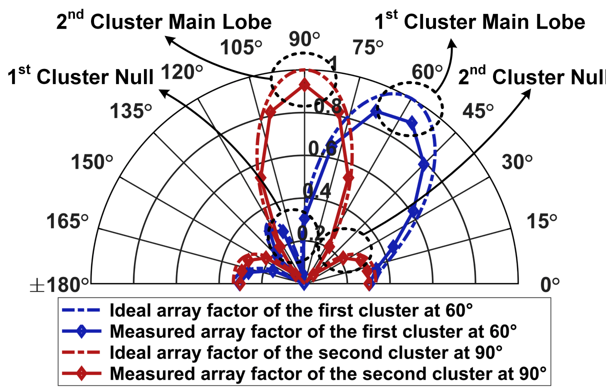

Figure 5.3: measured spatially multiplexed array factors of 2 clusters (ideal array factors are shown in dashed) steered concurrently toward 60° and 90°

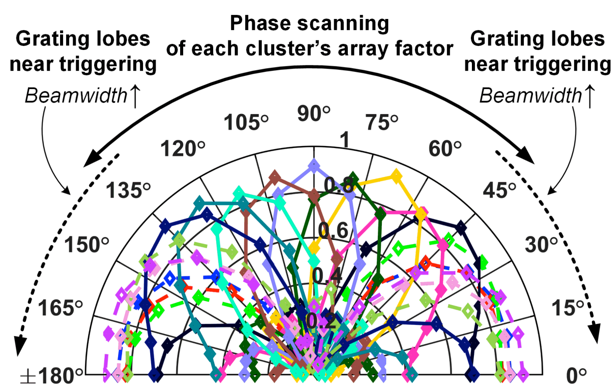

Figure 5.4: measured phase scanning of array factor of each 3-element cluster

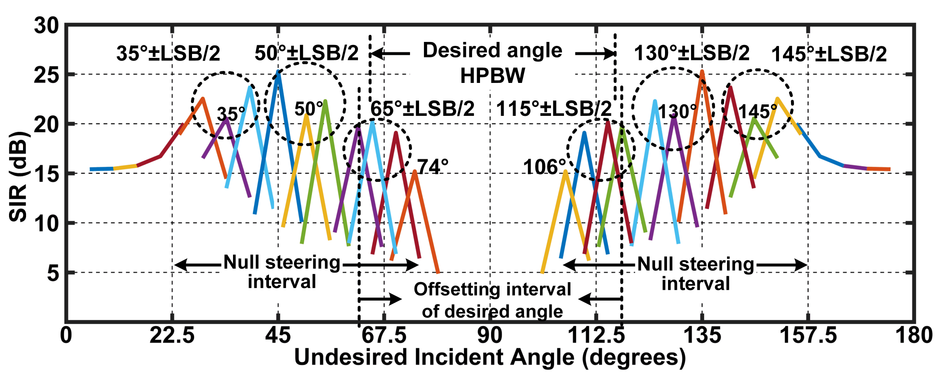

Figure 5.5: Measured signal-to-interference ratio (SIR) of a cluster steered toward broadside with interference incident angle swept from 5° to 175°

Chapter 6

Conclusion

Figure 6.1 Shows the $3.5{\times}3\text{mm}^2$ die micrograph of the 4-element/6-channel RX prototype implemented in 130nm SiGe BiCMOS process. The comparison table with prior arts [2–5] is presented in table 6.1. For a comparable conversion gain, the proposed 4-element RX consumes lower DC power (88mW per RF-to-BB channel including LO and 2 Mixer-BB) while showing better NF (RF-to-BB DSB NF) and linearity. More importantly, a MIMO multiplexing gain of 2 is achieved in the proposed RX in contrast to no multiplexing gain in conventional phased array architectures. In conclusion, A 4-element RX architecture with simultaneous beamforming and MIMO capabilities both implemented in the RF domain were presented. By decomposing RX elements into 2 partially overlapped beamforming clusters with independent amplitude and phase control, the proposed RX achieves a higher MIMO multiplexing gain compared to conventional phased array or hybrid architectures with the same number of elements per cluster. Measurement results were presented showing excellent agreement with simulation, while verifying the system-level feature of concurrent spatial multiplexing and interference rejection.

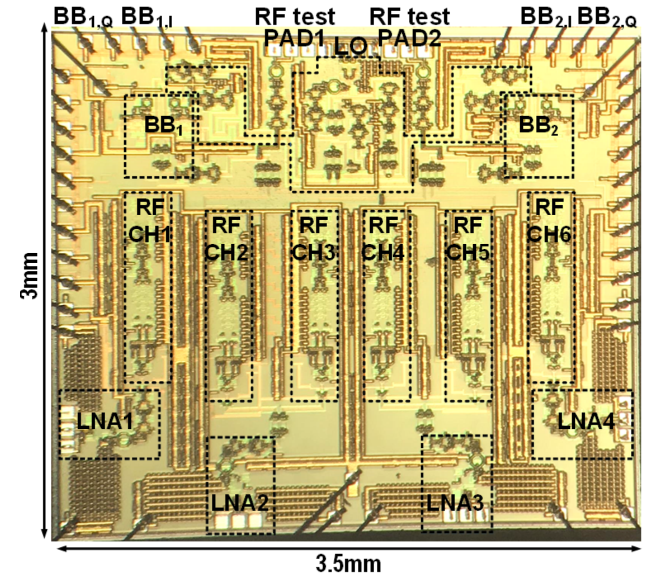

Figure 6.1: Die micrograph of the propopsed 4-element RX

		ISSCC 2017 [2]	TMTT 2017 [3]	JSSC 2012 [4]	TMTT 2013 [5]	This Work
Architecture		**TRX** Phased Array	**TRX** Phased Array	**RX** Phased Array	**RX** Phased Array	**RX** Phased Array MIMO
Phase Shifting		RF	LO	RF	RF	RF
Process		130nm	90nm	130nm	130nm	130nm
# of Channels		16	4	4	16	6
Integration		RF/LO/BB	RF/LO/BB	RF	RF/LO/BB	RF/LO/BB
Frequency (GHz)		27-29	71-86	76-84	76-84	64-67
Max Conv. Gain (dB)		34	26.2	10.1-18.9	30-33	30.15
Channel NF(dB)		6 *	9-14	10-11	11.4-13	9.8-11 †
Gain Control (dB)		8	-	9	11.2	11
Input P1dB (dBm)		-22.5	-30.6	-26.7	-23	-16.3
P_{DC} (mw)		3300	286 **	130 **	1200	528 ††
MIMO Capability	**MUX. Gain**	**NA**	**NA**	**NA**	**NA**	**2**
	Streams	**1**	**1**	**1**	**1**	**2**

* NF of LNA+ front-end switch only ** P_{DC} per RF channel

† NF of the complete chain (RF to BB)

†† P_{DC} of all channels for 2-streams (including Mixer-BB-LO)

Table 6.1: Comparison table

Bibliography

[1] S. Mondal, R. Singh, A. I. Hussein, and J. Paramesh, “A 25-30 GHz 8-antenna 2-stream hybrid beamforming receiver for MIMO communication,” in *2017 IEEE Radio Frequency Integrated Circuits Symposium (RFIC)*, June 2017, pp. 112–115.

[2] B. Sadhu and et al, “7.2 A 28GHz 32-element phased-array transceiver IC with concurrent dual polarized beams and 1.4 degree beam-steering resolution for 5G communication,” in *2017 IEEE International Solid-State Circuits Conference (ISSCC)*, Feb 2017, pp. 128–129.

[3] N. Ebrahimi, P. Wu, M. Bagheri, and J. F. Buckwalter, “A 71-86-GHz Phased Array Transceiver Using Wideband Injection-Locked Oscillator Phase Shifters,” *IEEE Transactions on Microwave Theory and Techniques*, vol. 65, no. 2, pp. 346–361, Feb 2017.

[4] S. Y. Kim and G. M. Rebeiz, “A Low-Power BiCMOS 4-Element Phased Array Receiver for 76-84 GHz Radars and Communication Systems,” *IEEE Journal of Solid-State Circuits*, vol. 47, no. 2, pp. 359–367, Feb 2012.

[5] S. Y. Kim, O. Inac, C. Kim, and G. M. Rebeiz, “A 76-84 GHz 16-element phased array receiver with a chip-level built-in-self-test system,” in *2012 IEEE Radio Frequency Integrated Circuits Symposium*, June 2012, pp. 127–130.

[6] H. Mohammadnezhad, A. K. Bidhendi, M. M. Green, and P. Heydari, “A low-power BiCMOS 50 Gbps Gm-boosted dual-feedback transimpedance amplifier,” in *2015 IEEE Bipolar/BiCMOS Circuits and Technology Meeting - BCTM*, Oct 2015, pp. 161–164.

[7] A. Karimi-Bidhendi, H. Mohammadnezhad, M. M. Green, and P. Heydari, “A Silicon-Based Low-Power Broadband Transimpedance Amplifier,” *IEEE Transactions on Circuits and Systems I: Regular Papers*, vol. 65, no. 2, pp. 498–509, Feb 2018.

[8] H. Mohammadnezhad, H. Wang, and P. Heydari, “Analysis and Design of a Wideband, Balun-Based, Differential Power Splitter at mm-Wave,” *IEEE Transactions on Circuits and Systems II: Express Briefs*, vol. 65, no. 11, pp. 1629–1633, Nov 2018.

[9] H. Mohammadnezhad, R. Abedi, A. Esmaili, and P. Heydari, “A 64-67GHz partially-overlapped phase-amplitude-controlled 4-element beamforming-MIMO receiver,” in *2018 IEEE Custom Integrated Circuits Conference (CICC)*, April 2018, pp. 1–4.

[10] M. Lee, A. Karimi-Bidhendi, O. Malekzadeh-Arasteh, P. T. Wang, Z. Nenadic, A. H. Do, and P. Heydari, "A CMOS inductorless MedRadio OOK transceiver with a 42 μW event-driven supply-modulated RX and a 14% efficiency TX for medical implants," in *2018 IEEE Custom Integrated Circuits Conference (CICC)*, April 2018, pp. 1–4.

[11] E. Bjrnson, M. Matthaiou, and M. Debbah, "Massive MIMO with Non-Ideal Arbitrary Arrays: Hardware Scaling Laws and Circuit-Aware Design," *IEEE Transactions on Wireless Communications*, vol. 14, no. 8, pp. 4353–4368, Aug 2015.

[12] J. Mo and R. W. Heath, "High SNR capacity of millimeter wave MIMO systems with one-bit quantization," in *2014 Information Theory and Applications Workshop (ITA)*, Feb 2014, pp. 1–5.

[13] H. Pirzadeh and A. L. Swindlehurst, "Spectral Efficiency of Mixed-ADC Massive MIMO," *IEEE Transactions on Signal Processing*, vol. 66, no. 13, pp. 3599–3613, July 2018.

[14] K. Roth, H. Pirzadeh, A. L. Swindlehurst, and J. A. Nossek, "A Comparison of Hybrid Beamforming and Digital Beamforming With Low-Resolution ADCs for Multiple Users and Imperfect CSI," *IEEE Journal of Selected Topics in Signal Processing*, vol. 12, no. 3, pp. 484–498, June 2018.

[15] A. Mahajan, A. K. Bidhendi, P. T. Wang, C. M. McCrimmon, C. Y. Liu, Z. Nenadic, A. H. Do, and P. Heydari, "A 64-channel ultra-low power bioelectric signal acquisition system for brain-computer interface," in *2015 IEEE Biomedical Circuits and Systems Conference (BioCAS)*, Oct 2015, pp. 1–4.